ADVANCED PHOTONICS RESEARCH
Open Access
www.adpr-journal.com

Nanostructure-Derived Antireflectivity in Leafhopper Brochosomes

Progna Banerjee, Gabriel R. Burks, Sarah B. Bialik, Mostafa Nassr, Elizabeth Bello, Marianne Alleyne, Benny D. Freeman, Jeffrey E. Barrick, Charles M. Schroeder, and Delia J. Milliron*

Understanding how insect-derived biomaterials interact with light has led to new advances and interdisciplinary insights in entomology and physics. Leafhoppers are insects that coat themselves with highly ordered biological nanostructures known as brochosomes. Brochosomes are thought to provide a range of protective properties to leafhoppers, such as hydrophobicity and antireflectivity, which has inspired the development of synthetic brochosomes that mimic their structures. Despite recent progress, the high antireflective properties of brochosome structures are not fully understood. Herein, a combination of experiments and computational modeling is used to understand the structure-, material-, and polarization-dependent optical properties of brochosomes modeled on the geometries found in three leafhopper species. The results qualitatively represent that light interference interaction with nanostructures naturally occurring in brochosomes is responsible for the spectral tuning and the asymmetric line shape of the reflectance spectra. Whereas prior work has focused on the computational modeling of idealized pitted particles, this work shows that light–matter interactions with brochosome structures can be tuned by varying the geometry of their cage-like nanoscale features and by changing the arrangement of multiparticle assemblies. Broadly, this work establishes principles for the guided design of new optically active materials inspired by these unique insect nanostructures.

1. Introduction

Light–matter interactions arise across various length scales[1] and are the driving force behind revolutionary technological advances such as optoelectronic devices[2] and solar cells.[3] Biology has evolved numerous examples of sophisticated light–matter interactions, such as those used in photosynthesis, to capture energy from light.[4] Insects are notable for the diversity of nanostructures with optical activity found on their cuticles, which have been reported to give rise to diffraction, interference, reflectance, and iridescence effects.[5] Such biological nanostructures often lead to striking visual phenomena, for example, the structural coloration[6] and iridescence of the wings of *Morpho* butterflies[7,8] are attributed to multiple slit interference effects from light interactions with periodic grating-like structures.

Insect surface structures exhibiting antireflectivity with angular and polarization dependence are often used for

P. Banerjee
Center for Nanoscale Materials (CNM)
Nanoscience and Technology (NST) Division
Argonne National Laboratory
Lemont, IL 60439, USA
E-mail: pbanerjee@anl.gov

P. Banerjee, M. Nassr, B. D. Freeman, D. J. Milliron
McKetta Department of Chemical Engineering
The University of Texas at Austin
Austin, TX 78712, USA

G. R. Burks, C. M. Schroeder
Department of Materials Science & Engineering
University of Illinois at Urbana-Champaign
Urbana, IL 61801, USA

The ORCID identification number(s) for the author(s) of this article can be found under https://doi.org/10.1002/adpr.202200343.

DOI: 10.1002/adpr.202200343

G. R. Burks, M. Alleyne, C. M. Schroeder
Beckman Institute for Advanced Science and Technology
University of Illinois at Urbana-Champaign
Urbana, IL 61801, USA

S. B. Bialik, J. E. Barrick
Department of Molecular Biosciences
The University of Texas at Austin
Austin, TX 78712, USA

E. Bello, M. Alleyne
Department of Entomology
University of Illinois at Urbana-Champaign
Urbana, IL 61801, USA

M. Alleyne
Department of Mechanical Science and Engineering
University of Illinois at Urbana-Champaign
Urbana, IL 61801, USA

C. M. Schroeder
Department of Chemical and Biomolecular Engineering
University of Illinois at Urbana-Champaign
Urbana, IL 61801, USA

camouflage.[9–11] Many of these reflectivity behaviors originate from structures that are highly ordered on the micron and nanometer scales. For example, the compound eyes and the wings of moths and other insects contain periodic nanopillars.[5,12] These arrays of nanostructures generate a gradual change in refractive index near the surface that leads to antireflectivity. However, disordered arrays of nanostructures can also result in antireflective properties as demonstrated by wing and eye structures[13] found in beetles, cicadas, and glasswing butterflies.[12] Besides its relevance in nature, light reflection is commonly encountered in optical device applications. Reflection decreases energy conversion efficiency in solar panels and limits the effectiveness of cloaking devices.

In this work, we study the antireflectivity associated with brochosomes and seek the underlying mechanism. Brochosomes are hollow, spherical nanostructures with diameters of hundreds of nanometers produced by leafhoppers (Hemiptera; Cicadellidae). Brochosome-inspired synthetic nanostructures were recently investigated for applications as antireflective coatings,[14–17] although it is not known to what extent natural brochosomes exhibit these properties and whether they have biological significance. Brochosomes have a cage-like morphology with pentagonal and hexagonal faces defined by struts surrounding open pits. At the molecular level, brochosomes consist mainly of proteins and lipids.[18] Brochosomes are produced by specialized cells located in the Malpighian tubules[19] of leafhoppers, then excreted and spread by the insects over their bodies where they adhere in irregular arrangements.

Natural brochosomes do not exhibit grating-like periodic lamellar structures or a regular spacing on leafhopper surfaces. Synthetic mimics of brochosomes exhibiting an ultra-high antireflective behavior across a broad spectral range have only been tested in periodic arrays.[14] Despite recent work, several unanswered questions remain regarding how the ordering of brochosome-coated surfaces impacts the reflectance behavior. In a recent study, Yang et al.[14] prepared synthetic brochosomes from colloidal templates and were able to tune the pit diameter to height ratios and the relative sizes of the brochosomal spheres to pit dimensions, observing that electrodeposited arrays of silver brochosomes exhibit appreciable antireflectivity. Despite this recent progress and theoretical work exploring the design space of brochosome-inspired[15] particle morphologies, we lack a full understanding of the mechanism of antireflectivity in brochosomes and how it depends on their internal structure and spatial organization.

To decipher this mechanism in brochosomes, we utilize mathematical modeling of light scattering in the near-field regime. Light scattering by objects with dimensions comparable to the wavelength of the incident radiation can be understood by studying variations in the intensity of the optical near field in the vicinity of the object, within an approximate distance of a wavelength from the surface. Many reactive and radiative phenomena occur in this range, such as scanning near-field optical microscopy (SNOM),[20] near-field tip-enhanced Raman scattering (TERS),[21] and other plasmon-enhanced interactions and applications.[22] These interactions occur with both dielectric materials[23,24] and mixed metal-dielectric media.[25] For leafhopper brochosomes, spatial variation of the optical near-field can reveal how their substructures and organization influence interactions with light, which ultimately determines far-field optical properties such as reflectivity. When the diameter D of a structure is greater than the wavelength λ, which is true from the UV through most of the visible region for brochosomes, the relation defining the reactive near-field region (defined by the distance R which is measured from outer surface of the brochosomes in this particular instance) is written as

$$R = 0.62 \times \left(\frac{D^3}{\lambda}\right)^{0.5} \quad (1)$$

With this analytical formulation and the polar counterpart,[26] one can predict how geometric features on a surface will influence the radiative patterns of both electric and magnetic dipoles in the selected spectral region. The incident field vector is expected to vary in phase, magnitude, and directionality over the material geometry in this range, causing fluctuating dipole moments in the material.

In this work, we study the mechanisms of light–matter interactions with brochosomes that lead to antireflectivity using a combination of experiments and simulations. We show that these interactions can be tuned by varying the geometry of their nanoscale features and by organizing into them in periodic or disordered assemblies. Furthermore, these antireflective properties are found to be material independent, which opens up opportunities for employing them in diverse biomimetic applications. Overall, these results establish new engineering design principles for developing nanostructured surfaces inspired by brochosomes.

2. Results and Discussion

2.1. Natural Brochosome Structures Modeled Using Composite Refractive Indices (Brochosomes and Air)

We began by studying light–matter interactions for nanostructures modeled after brochosomes using finite-element electrodynamics simulations in the near-field regime as calculated from Equation (1). Antireflective properties were simulated using experimentally extracted parameters from brochosome films through ellipsometry measurements- on structures that were modeled after the brochosomes found on the wings of *Balclutha rubrostriata* (**Figure 1**a), *Graminella* sp. (Figure 1e), and *Empoasca* sp. (Figure 1i). We then applied these refractive indices to study the various dimensional dependencies of antireflective properties on the species-specific brochosome diameters and the geometry and orientation of the pits. The *Graminella* sp. brochosomes in these samples have slightly larger pit sizes and distorted-hexagonal arrangements compared to brochosomes from *Balclutha rubrostriata*. Both types are roughly spherical in shape, whereas the *Empoasca* sp. brochosomes are oblong and have mostly pentagonal pits. Image analyses (Figure 1) of datasets acquired through electron microscopy were used to determine the geometric parameters used in the computational models. We chose to incorporate substructural details such as the struts defining the brochosome pits in our computational model. This choice was implemented to more faithfully reflect the natural brochosome architectures when compared to the pitted spheres considered in previous studies.[14] Using this approach, we modeled quantities such as spatially varying electric field

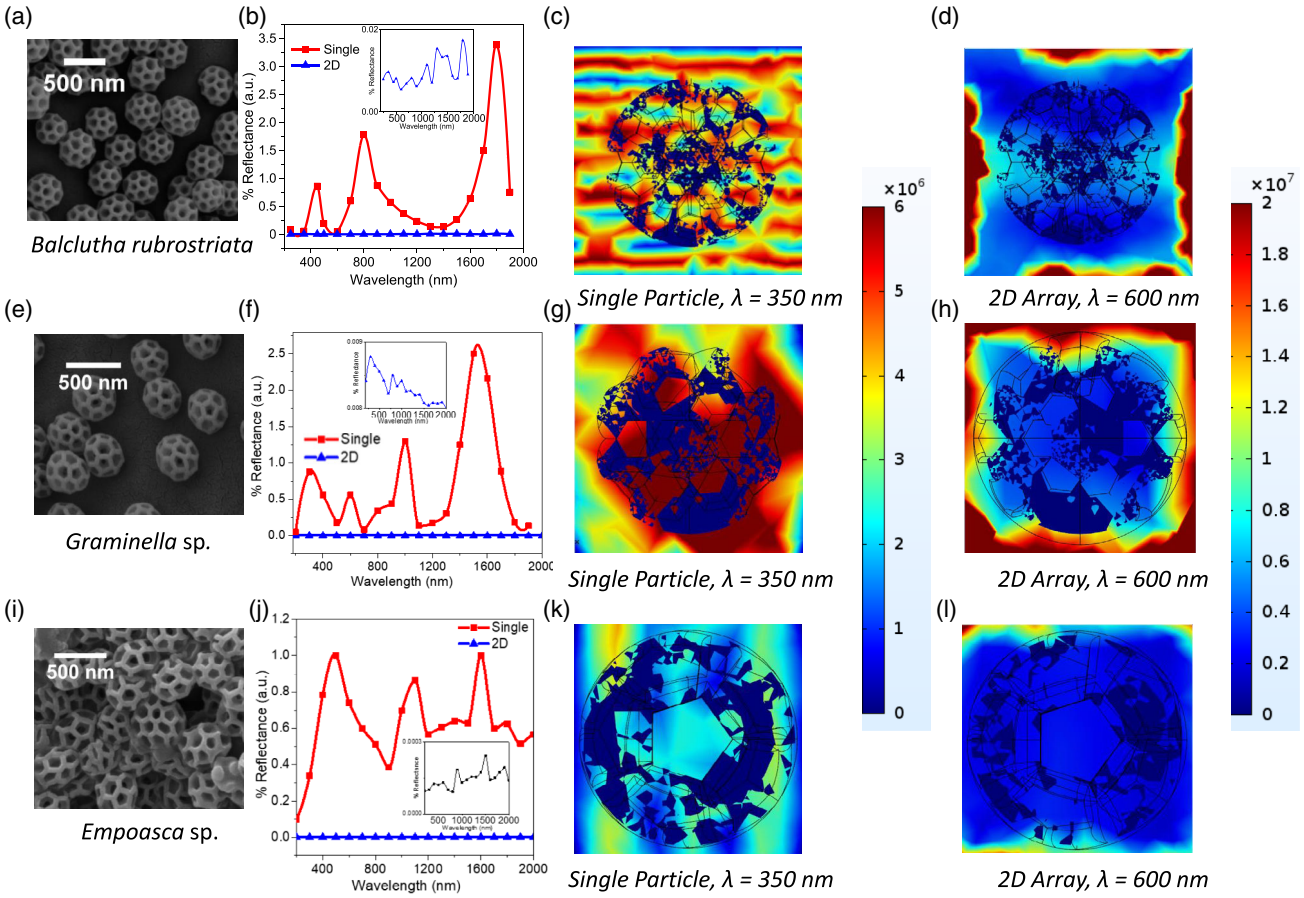

Figure 1. Representative electron microscopy images of brochosomes on the wing surfaces of a) *Balclutha rubrostriata*, e) *Graminella sp.*, and i) *Empoasca sp.* leafhoppers. b,f,j) Simulated reflectance spectra determined over the entire spectral region, 200–2000 nm, for morphologies modeled after each of these species are overlaid for a single, isolated brochosome and an ordered 2D array. The electric field intensity maps, modeled with the incident radiation traveling into the plane and calculated for the lateral components of the electric field over a section on the surface of the brochosome are shown in for a single brochosome and in d,h,l) for an ordered 2D assembly created with periodic boundary conditions applied along the lateral directions. The reflectance wavelength minima selected for the field maps shown in the figure were $\lambda = 350$ nm for single brochosomes, and $\lambda = 600$ nm for uniform 2D arrays, which exhibited strong electromagnetic field interactions across all species. Scale bars for the electric field color maps are identical for the single brochosomes (c,g,k) and for the arrays (d,h,l). Optical features and maps were simulated using the composite refractive indices (brochosomes and air) obtained experimentally from brochosome films through ellipsometry.

intensities, electric and magnetic dipoles, and the far-field specular and diffuse reflectivity with a spatial resolution of one nanometer over the brochosome structures.

2.2. Effect of Brochosome Geometry on the Optical Properties of Isolated Brochosomes

We first studied the optical behavior in single isolated brochosomes modeled after the brochosomes found on the wings of *Balclutha rubrostriata* (Figure 1a), *Graminella* sp. (Figure 1e), and *Empoasca* sp. (Figure 1i) leafhoppers to account for geometric variation among leafhopper species. The reflectance spectra and field distribution were found to strongly depend on both the brochosome and pit geometries. Incident radiation was simulated through the introduction of plane waves (6.199–0.6199 eV) impinging perpendicularly upon the surfaces of brochosomes, wherein we observe the resultant percentage reflectance values to vary within ≈1–4% for single brochosomes (Figure 1b,f,j). Peaks and valleys are observed in the reflectance spectra for brochosomes from all leafhopper species, though the reflectance extrema wavelengths and relative reflectance values at the maxima/minima vary with brochosomal geometry. The local near field is considered in all calculations in this study. This is because in this wavelength range defined by Equation (1), light can be thought of as consisting of plane waves. The local field can be approximated as a uniform spherical wave over the interacting material for most calculations across a specified reference area. This approach is taken in the physical models that have been used to understand optical tip-sample interactions in SNOM microscopy, for example.

Here, the ordering of the pits in a hexagonal arrangement, as in the single *Balclutha rubrostriata* and *Graminella sp.* brochosomes, appears to give rise to the quantitatively the largest peak value in the simulated reflectance spectrum (Figure 1c,g,k). The lowest peak reflectance value was obtained for the *Empoasca* sp.

brochosomes, which have the least symmetric pit shape and orientation. The peak positions for all maxima and minima in the reflectance spectra and their quantitative variations depend on the brochosomal geometry. Electric field intensity maps were calculated for single brochosomes to quantify the spatial (de)localization of the electromagnetic fields over brochosomal surfaces. The spatial electric field distribution varies from a homogeneous distribution spanning over and around ≈500 nm from the surface of the brochosome, part of which is shown in Figure 1, in particular, (Figure 1c), to a strongly localized field over ≈450 nm (Figure 1g), to a weakly localized field over part of the brochosome (Figure 1k), depending on the species-specific geometry. The red regions of the field maps, indicating the strongest calculated relative field enhancements $(|E|/|E_0|)^2$ of $\approx 2 \times 10^7$ are distributed uniformly over the surface of the *Balclutha rubrostriata* brochosome and near field (≈200 nm away from the surface). For the slightly asymmetric brochosome of the *Graminella sp.*, these field intensity "hot spots" are located over the central parts and thin out near the edges. For the asymmetric *Empoasca* sp. brochosomes, the field is relatively sparse, and uniformly distributed for the most part. Thus, using electrodynamic simulations we show the locations and numerical values of enhancement intensities of electric field hot spots around brochosomes interacting with incident light depend on their geometry.

A quantitative study of the size distributions of brochosomes obtained from these species is provided in Figure S1, Supporting Information. The role of brochosome diameter (250–750 nm) in influencing the quantitative and qualitative behavior of reflectance is explored in Figure S2, Supporting Information, for the *Empoasca sp.* and the Balclutha *rubrostriata,* respectively. It reveals that the increased size positively affects antireflective properties. Field maps obtained at 450 nm on the *Empoasca* sp. show that some sizes (350, 500 nm) produce more concentrated fields (higher antireflective properties) than others (250, 600 nm). The *B. rubrostriata* geometry generally shows a larger number of pits and shows a higher reflectance peak of up to 16% at the lower values of diameter (250 nm), which can be explained as the change in light interference maxima/minima that result in detuning pits as they are brought closer together. We, therefore, conclude that size does not directly impact reflectivity but may indirectly do so if the pit spacing changes.

2.3. Effect of Disorder on Optical Properties in Brochosome Arrangements

In addition to understanding the near-field behavior of individual brochosomes, assemblies of such brochosomes were simulated using periodic and disorganized arrays, respectively. Uniform periodic arrays of brochosomes in the lateral directions yield negligible reflectance values (0.00001–0.02% shown in Figure 1b,f,j) over the spectral range. Electric field intensity maps were calculated for both the periodic arrays of brochosomes, and asymmetric assemblies of brochosomes to quantify the spatial (de) localization of the electromagnetic fields over brochosomal surfaces. The light scattered from 2D uniform brochosome arrays forms localized bands positioned between the brochosomes due to interference of scattered waves, as shown in red regions for Figure 1d,h,l for ordered arrays.

When compared to maps from individual brochosomes obtained at (300, 1400 nm) (**Figure 2**a,d) representing valleys (dips), and (450, 750 nm) (Figure 2b,c) selected for peaks; we confirm the electromagnetic fields are mainly localized over the surface of individual brochosomes within the distance defined by Equation (1). For demonstration purposes in the figures, these maps are shown as a stack of semitransparent slices through the top-half of the brochosomal hemisphere placed atop one another, to provide a deeper understanding of the 3D distribution. Results are next shown for brochosomes in a regular 2D array (Figure 2e–h) with a similar map representation procedure followed for the reflectance peak minima (e,h) and maxima (f,g). In summary, uniform brochosome arrays result in a weaker dependence of field enhancements immediately surrounding the brochosomes when compared to maps obtained at similar maxima and minima for single brochosomes.

We next investigated the interactions between brochosomes placed in disordered arrays with various spatial arrangements (Figure 2i–t: disordered arrays). We varied the interbrochosomal distances and packing fractions in these configurations based on electron microscopy images (Figure 2: left inset of i,j,k respectively, and S3, Supporting Information**)**. The respective packing fractions of these three cases are: Figure 2i: 0.48 Figure 2m: 0.57, and Figure 2q: 0.76. Brochosomes were placed far apart from each other (defined by an interbrochosomal distance of ≈100 nm), as shown in the configurations in Figure 2i–l, to observe the subsequent effects on reflectance and field intensity distributions. The resulting reflectance maps demonstrate a quantitatively intense field distribution of $\approx 4 \times 10^6\ \mathrm{V\,m^{-1}}$ for the valleys (350 and 1400 nm, Figure 2i,l).

When the disordered arrangement of brochosomes is brought successively closer together to form a sparse configuration (Figure 2m-p few of the brochosomes are closer than ≈10 nm), followed by progression to a denser configuration (Figure 2q–t), the system retains a pattern similar to a single brochosome wherein the spectral peaks (valleys) are characterized with delocalized (localized), low (high) intensity fields. Here, the sparse configuration results in the field mainly centered on the brochosomes for the valleys (300 and 1400 nm, Figure 2m,p), and the peaks show low near-field intensities of $\approx 1 \times 10^5\ \mathrm{V\,m^{-1}}$ of interactions (400 and 700 nm, Figure 2n,o). The relatively denser configuration of brochosomes with several of these touching, leads to an overall increase in field magnitude compared to the previous cases. Nevertheless, the same pattern emerges with the field growing weaker near the peaks (700 and 1450 nm, Figure 2r,s, corresponding to $\approx 10^5\ \mathrm{V\,m^{-1}}$) compared to the valleys (300, 1850 nm, Figure 2q,t, corresponding to $\approx 10^6\ \mathrm{V\,m^{-1}}$). Reflectance spectra for all configurations are shown in Figure 2u, with the maxima/minima tabulated in Table S1, Supporting Information.

We next performed in-depth studies of structure–property relationships to establish the importance of the pit geometry, i.e., the pit height, diameter, aspect ratio (height: diameter); and the relative orientation atop the brochosomes on these optical quantities. Detailed brochosome and pit dimensions are studied in Figure S4, Supporting Information, for the *Empoasca* sp. using atomic force microscopy to look at the cross-sectional details of these hollow pits. We report a pit depth of approximately 70 nm for the total brochosome diameter of 470 nm. Each pit has the nearest neighbors arranged in either

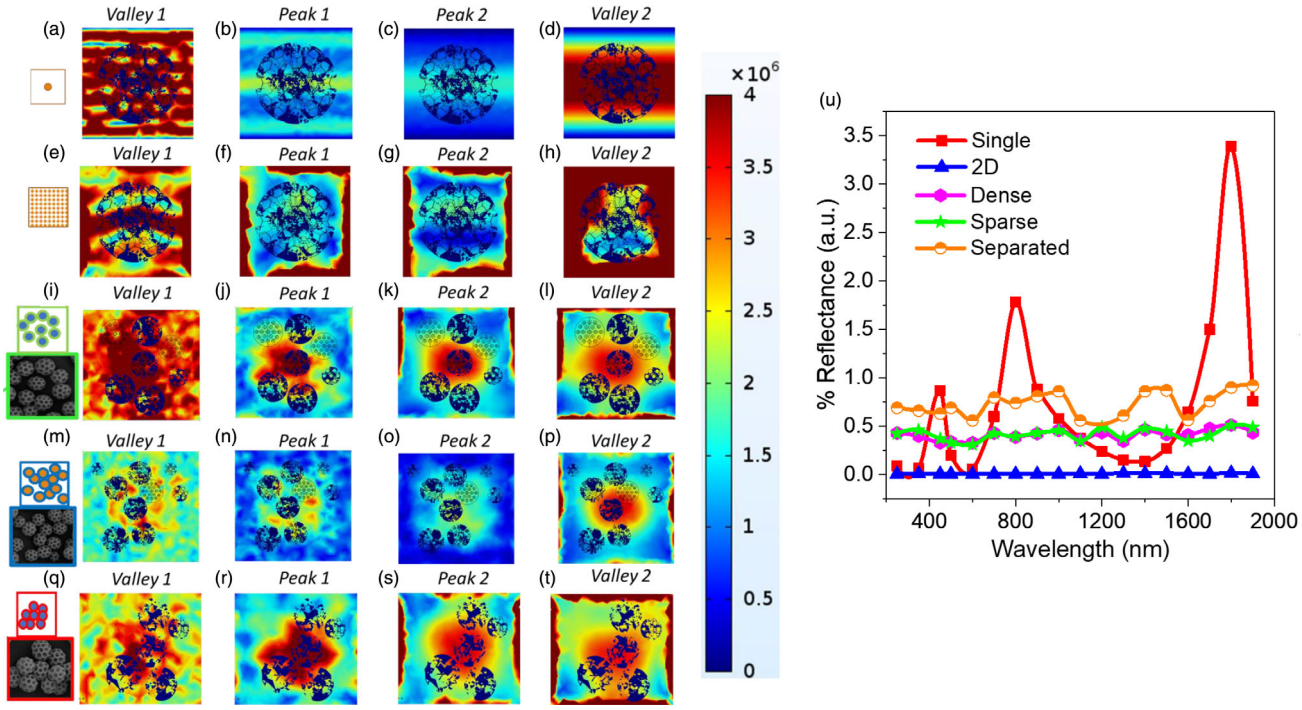

Figure 2. Simulated electric field intensities along the lateral directions over a cross-section on the surface created when brochosomes modeled on *Balclutha rubrostriata* are assembled in various formations. All scale bars denoting the field intensities for all panels in this figure are identical. a–d) Field intensity maps demonstrated for a single brochosome placed in the direct path of the incident radiation and excited over the entire spectral range (Figure 2u, red spectrum), where the maps were extracted for the peak extrema obtained from the reflectance spectra. The maps at 300 and 1400 nm (a,d) represent valleys (dips), while those at 450 and 750 nm excitation (b,c) provide peaks. The electric field distribution is of lower magnitude for the corresponding peaks in the reflectance spectra and vice versa. This trend is also observed for assemblies of brochosomes. e–h) A uniform 2D periodic array is simulated in the lateral directions. The maps corresponding to the peaks in the reflectance spectra (Figure 2u, blue spectra) at 750 and 1100 nm (f,g) show a lower quantitative value of field distribution and a uniform spatial distribution compared to the valleys taken from the spectra at 450 and 1900 nm (e,h), respectively. j–t) Proceeding as before, the heterogeneous assemblies of brochosomes were studied by bringing these together from far apart (i–l; peaks at i-350 and l-1850 nm, valleys at j-700 nm and k-1450 nm), to closer (m–p; peaks at m-300 and p-1400 nm, valleys at n-400 nm and o-700 nm) to a compact configuration (q–t; peaks at q-300 and t-1850 nm, valleys at r-700 nm and s-1450 nm). Each of the comparisons of the field maps at the peaks and valleys correspond to lower and higher field intensities delocalized/localized over the brochosomes. Scale bars for the field intensities in all panels of this figure are identical. u) Reflectance spectra for various configurations are shown. Optical features and maps were simulated using the composite refractive indices (brochosomes and air) obtained experimentally from brochosome films through ellipsometry studies described later in this study.

pentagonal (*Empoasca* sp.) or hexagonal patterns (*Macrosteles quadrilineatus, Balclutha rubrostriata,* and *Graminella sp*).

Overall, these simulation results show that the hot spots signifying the near-field intensities in brochosomes can be tuned through interbrochosomal arrangements, with spatial confinement being most pronounced for the single and sparsely placed brochosomes (within distance defined by Equation (1), to progressively being delocalized away from the brochosomes in the midst of the assembly as these are brought closer together. This behavior strongly points to the collective nature of the interaction giving rise to reflectance in brochosomes.

3. Explanation of the Optical Effects Using Optical Interference Between Light Scattered from Brochosome Pits and Ridges

Based on these results, we hypothesized that interference between scattered light may explain the reflectance patterns observed when radiation interacts with brochosome morphologies at the nanoscale. Identifiable interference features in this phenomenon are the presence of spectrally tunable extinction features with narrow and asymmetric line shapes occurring from the interference between the "bright" and "dark" modes, which refer to strong coupling to incident radiation and short radiative lifetimes, respectively. As explained in the following paragraphs and **Figure 3** in detail, light interference in the brochosomes arises from incident light being scattered from the nanostructures (pits and ridges of the brochosomes)-which interfere among themselves to form the reflectance peaks and valleys, respectively.

To determine whether the peaks and valleys in reflectance spectra (Figure 1 and 2) are tunable with geometry, and hence consistent with the concept of optical interference arising from coupling between scattered field components interacting with various pits; we thus varied the geometric relationship between the pits. The pits (shown for the unperturbed case in Figure 3a), which receive the full incident radiation are then shrunk or

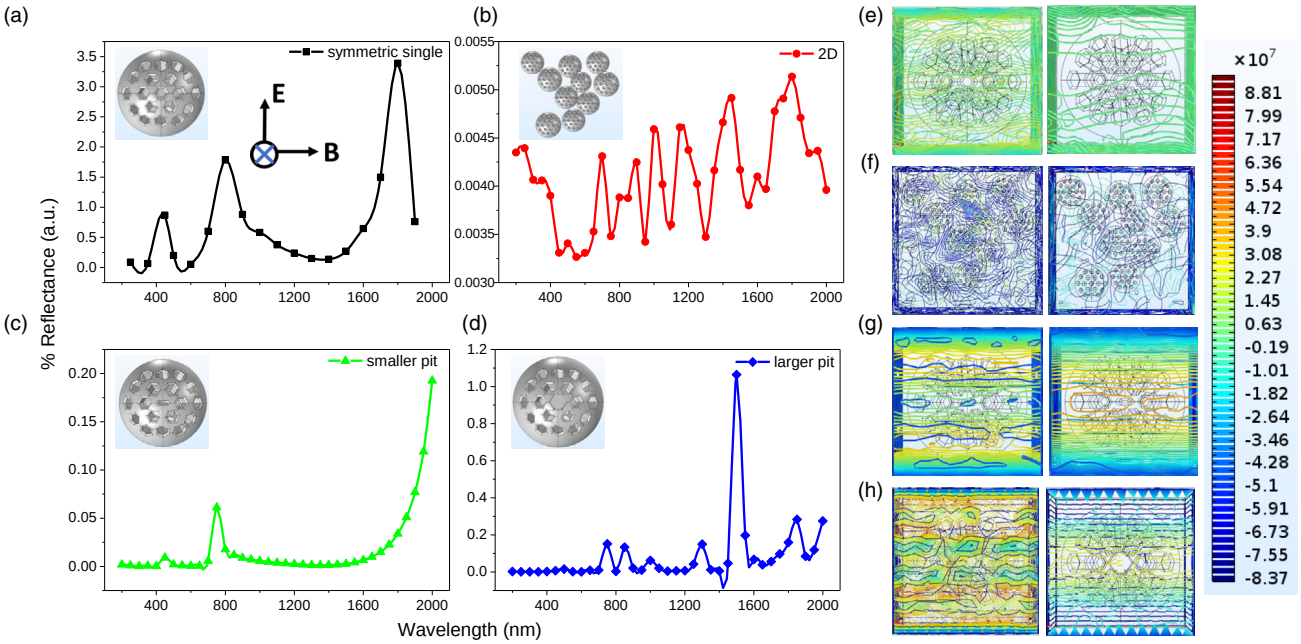

Figure 3. Simulated reflectance spectra determined for brochosome-inspired structures with the central pit geometry tuned to introduce variable separations with the surrounding pits. Reflectance spectra for the structures with the a) symmetric pit arrangement, b) disordered assembly containing randomized pit arrangements, c) reduced central pit, and d) expanded central pit are compared. The electric dipole contour maps for these cases are shown in (e–h) corresponding to (a–d), respectively, for excitation wavelengths selected for a peak (LEFT series of maps: a-450 nm, b-700 nm, c-750 nm, d-1,520 nm) and a selected valley (RIGHT series of maps: a-480 nm, b-600 nm, c-750 nm, d-1,400 nm, respectively). Optical features and maps were simulated using the composite refractive indices (brochosomes and air) obtained experimentally from brochosome films through ellipsometry studies.

expanded to create a larger or smaller distance respectively in relation to the neighboring pits (Figure 3c,d). An array of brochosomes with unperturbed pits are also shown in Figure 3b for comparison. The features in the reflectance spectra nearly vanish when the central pit has smaller dimensions (Figure 3c) and is therefore further away from its neighbors. The reflectance spectra change into sharper features (Figure 3d) for the larger central pit with smaller distances from its neighbors. These results suggest that the pit spacings dictate the spectral features, which is consistent with our hypothesis that optical interference is a primary factor determining reflectance behavior.

Contour maps depicting the dipole densities that are a direct qualitative visualization of the electromagnetic field, are observed to be homogeneously distributed for a single brochosome with unperturbed pits and for the array (Figure 3e,f respectively). The dipole density distribution decrease in absolute value for the vanishing reflectance spectral features from the smallest pit (Figure 3g). In contrast, for the largest pit (Figure 3h), the dipole density distribution in the contour map shows a marked increase in magnitude, visualized as red and green striations occurring in concentrated smaller regions over the brochosome for the reflectance minima (Figure 3h left plot). For the reflectance maxima (right plot of Figure 3h), the dipole density striations are observed to move away from the center because of out-of-phase between scattered radiations. The opposite behavior in the left and right maps in Figure 3g (left plot: blue/green striations of uniform low intensity, right plot: red striations concentrated in smaller regions near the center) is due to the weaker interference at the reflectance minima. Increased electric dipole contributions are correlated to the "bright" modes/sharper peaks observed in studies with interference, and "dark" modes/weaker peaks are thought to be contributions from the combined effects of the magnetic dipoles and electric quadrupoles.[27–31]

We next sought to understand how the reflective properties depend on the particle geometries and locations of the pits (Figure S5 and S6, Supporting Information). We analyzed brochosome-inspired structures consisting of spheres with hemispherical pits. These simulations were performed with Ag, a popular material for optical coatings and for bioinspired optical materials, to systematically elucidate the influence of substructure. A sphere containing 15 pits equally spaced across its upper surface (Figure S5a, Supporting Information) was compared to a sphere containing a subset of seven of these pits all located together on the top side facing the reader (Figure S5b, Supporting Information). The pits are spherical in shape and equally sized with one placed at the center surrounded with six pits, and eight more around the circumference so the periphery of the brochosomal model will contain indentations in Figure S5a, Supporting Information. The geometry in Figure S5b, Supporting Information, has one central pit and six more surrounding it while avoiding the periphery. The electric field intensity is vanishingly small over the surface of the smooth sphere as expected for a metal object, whereas the pits show the presence of localized electric field intensities (Figure S5c,d, Supporting Information). For pits closer to the equatorial region (Figure S5c, Supporting Information), the field intensity is closer to the maximum due to the topography of the curved surface. Application of periodic boundary conditions to the brochosomes

results in a decrease in the quantitative distribution of the electric field intensity (Figure S5g–j, Supporting Information). Pit aspect ratios for diameter over depth (Figure S6, Supporting Information) affect the optical properties in those certain combinations (2:1, 4.88:1, 4.28:1) produce quantitatively higher antireflective effects.

Simulations of dipole distributions using the quantified dipole density maps in our toy model (Figure S7 and S8, Supporting Information) are consistent with interference as the driving mechanism in structure-dependent antireflective behavior in brochosomes. The general theory of interference is discussed through the lens of scattering centers present on the leafhopper brochosomes in Figure S7, Supporting Information. Toy model using the generated spatial electromagnetic field distribution upon light-matter interaction on brochosomes, and the relative interference between electromagnetic waves producing the peak/valley effects are discussed in detail (Figure S8, Supporting Information).

By systematically varying brochosome structures, our results show that the pit geometries, pit locations and distributions, brochosome sizes, and arrangements are important defining factors determining the intensities and spatial and spectral locations of near-field hot spots of scattered light.

4. Comparison of Optical Property Simulations with Experiments

We next performed experimental measurements on brochosomes to determine the reflectance from the spectral and diffuse components using a spectrophotometer and the contributions of the *s* and the *p*-polarized components using an ellipsometer. Here, purified brochosomes from *Macrosteles quadrilineatus* were studied in the form of a thin film on a clean SiO_2 substrate (Methods), with reference for the reflectivity spectra obtained on blank SiO_2 substrates. **Figure 4**a shows a representative electron microscopy image of thin films of brochosomes in random orientations a few layers thick. Reflectance of single brochosome is represented by the simulation (Figure 4b) and experimental data from a thin film prepared with the brochosomes (Figure 4c), respectively. The simulation in Figure 4b, performed with plane wave incident light along similar viewing angles on a single brochosome of *M. quadrilineatus*, is used to understand the trend in the experimental oscillatory patterns of reflectance that show increasing amplitude near the IR. We then experimentally determined the total percentage reflectance of the combined specular and diffuse components using a diffuse reflectance accessory in a spectrophotometer as shown in Figure 4c. Reflectance spectra obtained from thin films of brochosomes from separate purified batches of *M. quadrilineatus* deposited on clean Si substrates are shown over the spectral range in Figure 4c. The peak ratios in Figure 4c are dependent on the randomized orientations presented by the assembly of the brochosomes in the experimental study. Low wavelength peaks are found in the experimental sample around the 450 nm region. Whereas the peaks typically observed from the single brochosome at the 750 nm and the 1,100 nm regions are contained within a larger envelope in the spectrum from Figure 4c. Moreover, we observe broad features in the near-IR region of the spectra, which can be explained as randomly oriented brochosomes in the thin films encountering incoming radiation at various angles of incidence. In a single brochosome, the angles of incidence can be thought of as a range of values originating from light hitting the structural elements of the brochosome, namely, the pits and the ridges at different locations over the curved

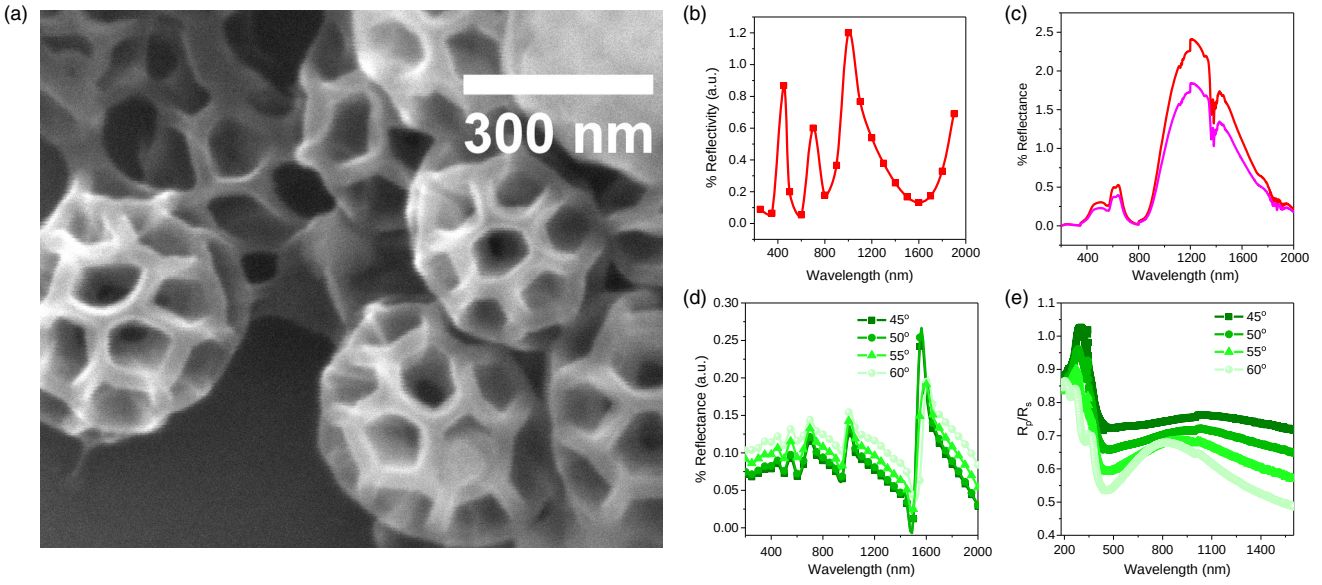

Figure 4. a) Electron microscopy image of a thin film of *M. quadrilineatus* brochosomes in random orientations. b) Reflectance of a single brochosome obtained by simulation. c) Experimental results for the combined specular and diffuse percent reflectance of such films (pink and red curve obtained from two separately prepared thin films show the reproducibility in the observed patterns). d) Simulations calculating the total percentage reflectivity show oscillatory behavior with increasing amplitude in the IR. e) Reflectivity measurements at specific angles, with respect to the normal, yield the shown ratio of the p/s polarized reflectivity.

surface. Summing up the contributions of scattered light expressed in terms of phases that originate from these pits and ridges would constitute a complex range as well. Next, putting into account the contributions from an ensemble of brochosomes with randomized arrangements from a film would definitely produce a complex interference which shows up in the experimental spectra as the broad features.

Ellipsometry was next used to determine the reflectance response of disordered assemblies of brochosomes to the specific polarization of incident light, and the angle of incidence was varied from 45° to 60° in 5° intervals. The thickness of the films, the incidence angle, and the measured angular parameters are used to determine Fresnel parameters R_p, R_s, and the real and imaginary indices n and k. When comparing ellipsometry simulation (Figure 4d) and experiments (Figure 4e), we see a broadening of the latter in the near-IR, which we interpret as heterogeneous broadening of the more distinct oscillatory trends arising from each brochosome under an envelope in the experimental results. The specular reflectance spectra (Figure 4d) show an angle-dependent resonant pattern emerging in the near-IR. The fraction of the incident radiation affecting the brochosome domain (in the case of simulations) or surface area (for the experiments) is inversely proportional to the angle of incidence. The ratio of R_p/R_s shows an initial decrease in magnitude followed by a broad peak emerging in the near-IR with increasing incidence angles (Figure 4e). The raw data obtained from the ellipsometry studies are plotted in Figure S9, Supporting Information, along with the fits obtained from the model described in Section SI2, Supporting Information, the derived parameters n and k are plotted in Figure S10, Supporting Information, and tabulated in Table S2, Supporting Information.

Field maps corresponding to the incident angles are shown in Figure S11, Supporting Information, where we observe new "quantized modes" corresponding to localized field hot spots that emerge/disappear with changes in the viewing angles. Quantized in this situation refers to the hot spot localization pattern and the spatial distribution changes with the viewing angle. A theoretical comparison of the components of specular and diffuse reflectance shows the latter to be negligible (Figure S12, Supporting Information). The contribution from the diffuse reflectance calculated over the spectral range is disproportionately smaller in magnitude compared to the specular signal. The variation of the diffuse component is limited mostly to the NIR.

5. Effect of Material on Optical Properties in Brochosomes Modeled After Natural Structures

We next examined the effect of material composition on the reflectivity of the brochosomal assemblies, with the detailed morphological specifications taken into account (**Figure 5**a–d) using simulations. Using the refractive index parameters of chitin-based material commonly found in various species of insects and arthropods[6,8,32] to further generalize the scope of material properties, the reflectance spectra of the 2D assemblies of

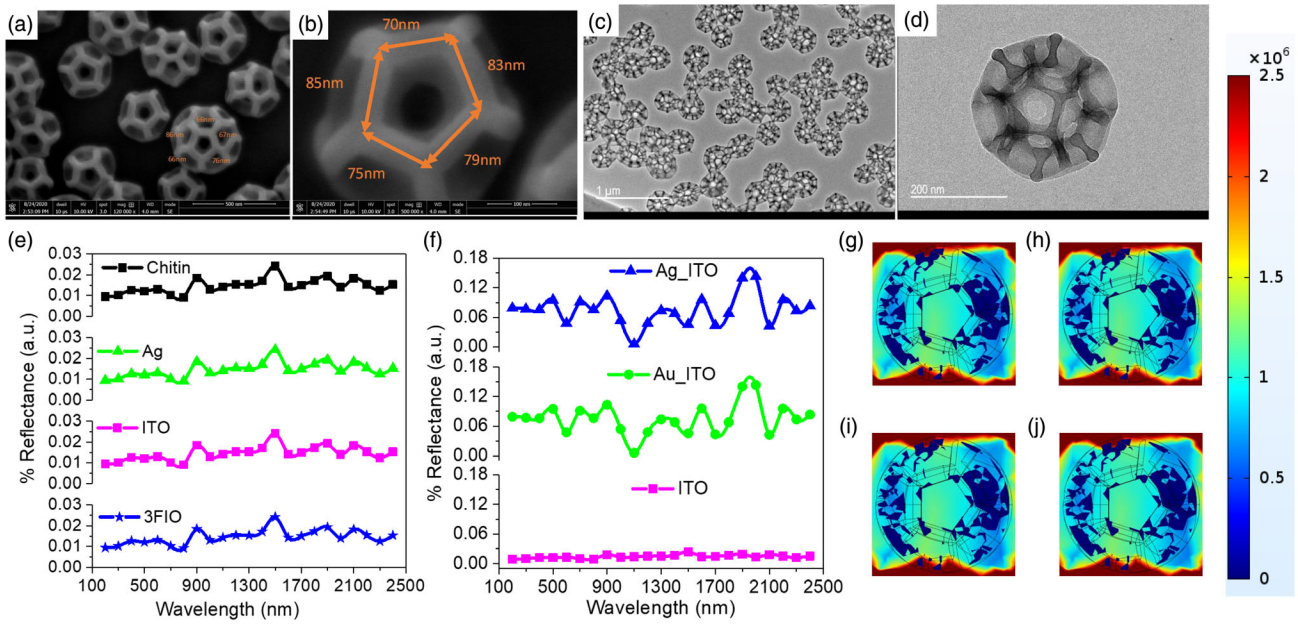

Figure 5. Dependence of simulated reflectance spectra on material composition of particles with brochosome geometries, including electron microscopy results from *Empoasca* sp. a) Free-standing brochosomes imaged via SEM showing brochosomal pits, axes, and two distinct brochosome sizes (350 and 500 nm). b) Magnified SEM image of 350 nm diameter brochosome with labeled axis lengths. c) TEM image of drop cast solution of brochosomes. d) High-magnification TEM image of single brochosome showing structural dimensionality of brochosomes and contrast confirming hollow brochosome structures. e) Reflectance spectra show negligible quantitative and qualitative changes when the material being simulated is chitin, silver, 10%-tin-doped indium oxide, or 3%-fluorine-doped indium oxide. f) When pits are filled in with Ag or Au with the base material as 10%-tin-doped indium oxide, reflectance increases. g–j) Corresponding field maps at 900 nm show that material composition does not affect light-matter interactions in the near-field. The ridges of the brochosome structure contribute to the overall reflectivity in addition to the pit substructures.

brochosomes were compared to the cases where silver, 10% tin-doped indium oxide, and 3% fluorine-doped indium oxide were used to model the material properties (Figure 5e). Chitin, a natural positively charged aminopolysaccharide, being one of the top most plentiful natural-based polymer behind cellulose is made of β-(1,4)-2-acetamido-2-deoxy-D-glucose[33] and mainly found in the exoskeletons of arthropods and yeasts. Chitin has been studied recently for its applications as a proton-conducting[34,35] biomaterial.

Our results show negligible differences in optical reflectance behavior and near-field intensity maps taken at 900 nm for the different materials studied here (Figure 5g–j). Structures were modeled (Figure S13, Supporting Information) with pit geometries on top of a hemisphere (a-d) or situated over a sphere (e-h) to understand the effects of the overall geometry of the brochosome in the design of artificial films. Minor changes in the quantitative and qualitative features of the field maps suggest that pits constructed in a hemispherical mold should suffice for applications. When the hollow pits of the brochosomes are filled in with metal silver (Figure S14, Supporting Information, for absorption spectra of Ag brochosomes) or gold, as in Figure 5f, there is a marked increase in the reflectance as expected from the loss of the scattering centers. Here, the ensuing structure will still contain the elevated struts, but will have the pits filled in. However, the elevated ridges present at the boundary of the pits provide secondary centers for scattering which still provide a low absolute value of reflectance across the spectral range. Interaction of light with brochosomes placed on top of substrates (Figure S15, Supporting Information) made of various materials shows little change in optical behavior.

Computational modeling was next performed for brochosomes immersed in liquid media. The liquids tested were selected because they span a range of refractive indices and are compatible with preserving brochosome structures in experimental studies (e.g., water, toluene, and oleic acid neither rupture nor otherwise degrade these brochosomes). When liquid fills the pits (Figure S16, Supporting Information), we observe the quantitative change in reflectance shows negligible dependence on the choice of the organic immersing media (water, toluene, oleic acid), as the scattering centers (pits in brochosomes) are lost to the interacting radiation. However, the overall quantitative value of the reflectance increases as a result of the loss of the pits as scattering centers upon immersing the structures in solvent media as compared to air (Figure S17, Supporting Information) by several orders up to ≈30%. These results are further evidence that the hollow pits of brochosomes are essential for maintaining their high antireflectance.

6. Conclusion

In this work, we explore the structure-optical property relationships in single brochosomes and assemblies both qualitatively and quantitatively, using a combination of electrodynamic simulations and optical experiments. The origin of the asymmetric line shapes in antireflective behavior in brochosomes is found to arise from the pits and struts on brochosome surfaces that serve as scattering centers of electromagnetic radiation. Aside from the structural effects, the values and positions of the extrema in reflectance spectra are shown to depend on the light polarization, incidence angle, near and far-field effects for the specular and the diffuse components, and the specific excitation frequencies.

The design lessons from our simulation studies are summarized as follows. Overall brochosome geometries (the diameter and number of pits were modified and their impact on the optical response were studied) can be tuned to shift the peaks in the reflectance spectra or to change the quantitative values within a few percent. The individual pit dimension alone does not affect the reflectance compared to the relative arrangements of pits atop brochosomes, which can be tuned to induce a broad band in the reflectance spectrum or several sharp peaks. Immersing brochosomes in liquid media is predicted to reduce their ultra-high antireflectivity by an order of magnitude due to loss of pits as scattering centers. Hemispherical brochosomes are indistinguishable from spherical structures, which facilitates and simplifies biomimetic synthetic design. Reflectance in brochosomal structures is angle dependent. The arrangement of brochosomes with close packing gives very well-defined peak and valley features in the corresponding reflectance spectra, with the emergence of electromagnetic hot spots on the surfaces of isolated brochosomes. Close proximity is more important in inducing these hot spots rather than order/disordered arrangements. For brochosomal assemblies, the electromagnetic field is stronger by an order of magnitude compared to single brochosomes, mainly in regions in between these structures. Finally, our results show that material choice is useful for modulating absorption features but does not appreciably affect antireflectance properties.

The material independence of the optical properties is an exciting finding that could potentially inspire the design of new synthetic antireflective materials. These functionalities may be envisioned to enable sensors, which, for example, would be used to induce directional reflectivity through the application of metamaterial designed with the structural guidelines put forth here. The guided design of metasurfaces and nanostructures is currently predicted using machine learning algorithms in inorganic architectures such as nanobars.[36] Using the design principles revealed from our work, developments are possible for bioinspired architectures and sensors using geometry as the primary tuning parameter for antireflectivity.

7. Experimental Section

Materials: Leafhoppers were collected in Texas and central Illinois by sweeping netting vegetation or by attracting insects to a black light. Individual insects were captured using mouth aspiration, frozen, and imaged for identification using a light microscope, followed by subsequent analysis.

Brochosome Purification: 20 leafhoppers (*Macrosteles quadrilineatus*) were placed in 25 mL of acetone for 25 min to extract brochosomes. The resulting suspension was sonicated following a protocol from Rakitov et al.[18] using a Bransonic 2800 digital bath for 3 min and then filtered using a 1 μm glass fiber syringe filter to remove the leafhoppers and isolate brochosomes. Several centrifugation runs were performed using a VWR high-speed Microcentrifuge at 16 000× g for 25 min to concentrate the brochosome solution.

Thin Film Preparation: A concentrated solution obtained from the purification protocol outlined above was dropped on a doped silicon wafer and the acetone was left to evaporate completely.

Electron Microscopy: Leafhopper wings of *Balclutha rubrostriata*, the *Graminella* sp., and *M. quadrilineatus* were imaged using scanning electron microscopy (SEM) to examine the brochosome nanostructures. Leafhopper wings were removed from insects and placed on a metal SEM stub with double-sided carbon tape and conductive graphite paint was placed next to the sample. The stub was subsequently sputter coated using platinum/palladium and examined using the Zeiss-Supra40-scanning electron microscope (Texas Material Institute, The University of Texas at Austin) at approximately 3–5 kV. Brochosomes of *Empoasca* sp. collected at Illinois were imaged via SEM using a FEI Quanta FEG 450 environmental scanning electron microscope (ESEM–Beckman Institute for Advanced Science and Technology, University of Illinois at Urbana-Champaign). For SEM imaging, brochosomes in acetone were drop deposited onto a glass substrate, dried, and sputter coated with gold/palladium. Transmission electron microscopy (TEM) imaging on brochosomes of the *Empoasca* sp. was performed using a JEOL JEM-2010 LaB_6 TEM (Materials Research Laboratory, University of Illinois at Urbana-Champaign). For TEM imaging, a dilute solution of free-standing brochosomes from the *Empoasca* sp. was drop deposited from acetone onto a Carbon-Formvar-coated TEM sample grid and imaged using a 200 kV electron beam. Brochosomes were found to be generally stable under the electron beam.

Atomic Force Microscopy: AFM imaging and analysis were conducted on brochosomes of *Empoasca* sp. with the Asylum Cypher AFM (Materials Research Laboratory at the University of Illinois at Urbana-Champaign). Samples were prepared as drop casted solution of free-standing brochosomes onto a glass substrate.

Ellipsometry Studies: The *s* and *p* components of reflectance of the purified thin films of brochosomes from *M. quadrilineatus* deposited on Si wafers were measured using a *M*-2000D model J.A. Wollam M2000 Spectroscopic Ellipsometer in the 200–1600 nm wavelength range. The angle of incidence varied between 45° and 60°, with an approximate beam size of 4 mm. The CompleteEASE software was utilized for data analysis and extraction of the refractive index parameters.

Spectrophotometer Studies: The reflectance of the purified thin films of brochosomes from *M. quadrilineatus* deposited on Si wafers was studied using an Agilent Cary series ultraviolet-visible-near infrared spectrophotometer with an additional diffuse reflectance accessory (DRA) installed. Operating in reflectance mode with the incident beam at an angle of ≈5°, the spectra were collected from 200 to 2000 nm for the measurement of the total (specular and diffuse) reflectance.

Electrodynamic Simulations and Theory: Finite element modeling (FEM) was used to model material geometries using a customized mesh shape and size tuned for fitting at the nanoscale-sized edges, faces, and corners of the geometries. Adaptive meshes were implemented using COMSOL (v 5.2) to enable control of the model architectures over grids with preset shapes, thereby improving near-field accuracy and decreasing computation time. Brochosomes were modeled as spheres into which polygonal pits are cut introduced following a hexagonal close-packed (hcp) pattern using binary operations. Brochosome architectures were then surrounded by a medium with the refractive index of air or liquids followed by determination of optical properties. Perfectly matched layers (PMLs) were used to absorb the evanescent waves at the boundary of the domain containing the geometries and including the ports giving out the incident plane waves. Collection ports were placed at the appropriate location in front of the PML to the incident port (for the specular reflection calculation), and around the domain at various collection angles in the far field (for the diffuse component calculation). A linearly polarized plane wave after scattering was converted into a scattered wave background field for calculating the diffuse components. Boundary conditions were then used for simulating the 2D periodicity using Floquet periodicity on the lateral directions, with the incident radiation as plane waves impinging on the geometry at normal incidence or at specific angles matching the experimental data. Material properties were modeled using the refractive indices for the Ag, 10% tin-doped indium oxide,[37–40] 3%-fluorine-doped indium oxide,[37] and chitin.[6,8,32] Reflectance spectra were measured from the global output of the S-parameters probed at the various collection ports. Near-field maps were obtained at a height equal to the topmost surface of the brochosomes.

Supporting Information

Supporting Information is available from the Wiley Online Library or from the author.

Acknowledgements

This research was supported by the Army Research Office (Project #: W911NF2020195). Work performed by P.B. at the Center for Nanoscale Materials, a Department of Energy Office of Science User Facility, was supported by the U.S. DOE, Office of Basic Energy Sciences, under Contract No. DE-AC02-06CH11357.

Conflict of Interest

The authors declare no conflict of interest.

Author Contributions

P.B. contributed through project conceptualization, establishing modeling methodology, optical simulations, and formal analysis using FEM-based electrodynamic software, and experimental optical studies, and wrote the original draft of the manuscript. G.R.B. performed transmission and atomic force microscopy experiments. S.B.B and G.R.B. performed scanning electron microscopy. S.B.B., J.E.B., E.B., M.A. collected leafhoppers. M.N. purified brochosomes and prepared films for experimental studies. D.J.M., C.M.S., M.A., J.E.B., and B.D.F. provided supervision and editing manuscript. All coauthors reviewed the manuscript.

Data Availability Statement

The data that support the findings of this study are available from the corresponding author upon reasonable request.

Keywords

antireflective materials, bioinspired, brochosomes, electrodynamic simulations interference

Received: January 29, 2023
Revised: March 25, 2023
Published online: May 7, 2023

[1] S. Rajabali, E. Cortese, M. Beck, S. De Liberato, J. Faist, G. Scalari, *Nat. Photonics* **2021**, *15*, 690.
[2] G. Eda, S. A. Maier, *ACS Nano* **2013**, *7*, 5660.
[3] A. Mihi, C. Zhang, P. V. Braun, *Angew. Chem. Int. Ed.* **2011**, *50*, 5712.
[4] P. Forn-Díaz, L. Lamata, E. Rico, J. Kono, E. Solano, *Rev. Mod. Phys.* **2019**, *91*, 025005.
[5] G. S. Watson, J. A. Watson, B. W. Cribb, *Annu. Rev. Entomol.* **2017**, *62*, 185.
[6] C. W. Mason, *J. Phys. Chem.* **1927**, *31*, 321.
[7] C. P. Barrera-Patiño, J. D. Vollet-Filho, R. G. Teixeira-Rosa, H. P. Quiroz, A. Dussan, N. M. Inada, V. S. Bagnato, R. R. Rey-González, *Sci. Rep.* **2020**, *10*, 5786.
[8] P. Vukusic, J. R. Sambles, C. R. Lawrence, R. J. Wootton, *Proc. R. Soc. B, Biol. Sci.* **1999**, *266*, 1403.

[9] F. Hischen, V. Reiswich, D. Kupsch, N. De Mecquenem, M. Riedel, M. Himmelsbach, A. Weth, E. Heiss, O. Armbruster, J. Heitz, W. Baumgartner, *Biol. Open* **2017**, *6*, 1209.
[10] R. C. Duarte, A. A. V. Flores, M. Stevens, *Philos. Trans. R. Soc. B, Biol. Sci.* **2017**, *372*, 20160342.
[11] K. Kjernsmo, H. M. Whitney, N. E. Scott-Samuel, J. R. Hall, H. Knowles, L. Talas, I. C. Cuthill, *Curr. Biol.* **2020**, *30*, 551.
[12] R. H. Siddique, G. Gomard, H. Hölscher, *Nat. Commun.* **2015**, *6*, 6909.
[13] A. Blagodatski, M. Kryuchkov, A. Sergeev, A. A. Klimov, M. R. Shcherbakov, G. A. Enin, V. L. Katanaev, *Sci. Rep.* **2014**, *4*, 6004.
[14] S. Yang, N. Sun, B. B. Stogin, J. Wang, Y. Huang, T.-S. Wong, *Nat. Commun.* **2017**, *8*, 1285.
[15] Z. Jakšić, M. Obradov, O. Jakšić, *Biomimetics* **2021**, *6*, 69.
[16] M.-S. Shih, H.-Y. Chen, P.-C. Li, H. Yang, *Appl. Surf. Sci.* **2020**, *532*, 147397.
[17] C. Hua, Z. Cheng, Y. Ma, H. He, G. Xu, Y. Liu, S. Yang, G. Han, *J. Electrochem. Soc.* **2021**, *168*, 042503.
[18] R. Rakitov, A. A. Moysa, A. T. Kopylov, S. A. Moshkovskii, R. S. Peters, K. Meusemann, B. Misof, C. H. Dietrich, K. P. Johnson, L. Podsiadlowski, K. K. O. Walden, *Insect Biochem. Mol. Biol.* **2018**, *94*, 10.
[19] R. A. Rakitov, *EJE* **2013**, *93*, 167.
[20] W. Zhang, Z. Fang, X. Zhu, *Chem. Rev.* **2017**, *117*, 5095.
[21] M. D. Sonntag, E. A. Pozzi, N. Jiang, M. C. Hersam, R. P. Van Duyne, *J. Phys. Chem. Lett.* **2014**, *5*, 3125.
[22] H. Yu, Y. Peng, Y. Yang, Z.-Y. Li, *npj Comput. Mater.* **2019**, *5*, 1.
[23] S. Lepeshov, Y. Kivshar, *ACS Photonics* **2018**, *5*, 2888.
[24] Yu. V. Vladimirova, V. G. Arakcheev, F. Song, V. N. Zadkov, *Phys. Rev. A* **2019**, *100*, 023847.
[25] T. Hutter, F. M. Huang, S. R. Elliott, S. Mahajan, *J. Phys. Chem. C* **2013**, *117*, 7784.
[26] P. Shankpal, V. Arur, G. Kadambi, J. Shuttleworth, *Int. J. Antennas Propag.* **2014**, *2014*, e958148.
[27] J. Parsons, E. Hendry, C. P. Burrows, B. Auguié, J. R. Sambles, W. L. Barnes, *Phys. Rev. B* **2009**, *79*, 073412.
[28] D. J. Cho, F. Wang, X. Zhang, Y. R. Shen, *Phys. Rev. B*, **2008**, *78*, 121101.
[29] A. Christ, Y. Ekinci, H. H. Solak, N. A. Gippius, S. G. Tikhodeev, O. J. F. Martin, *Phys. Rev. B* **2007**, *76*, 201405.
[30] T. Pakizeh, C. Langhammer, I. Zorić, P. Apell, M. Käll, *Nano Lett.* **2009**, *9*, 882.
[31] A. E. Miroshnichenko, Y. Kivshar, C. Etrich, T. Pertsch, R. Iliew, F. Lederer, *Phys. Rev. A* **2009**, *79*, 013809.
[32] D. Gur, B. Leshem, M. Pierantoni, V. Farstey, D. Oron, S. Weiner, L. Addadi, *J. Am. Chem. Soc.* **2015**, *137*, 8408.
[33] T. Naghdi, H. Golmohammadi, H. Yousefi, M. Hosseinifard, U. Kostiv, D. Horák, A. Merkoçi, *ACS Appl. Mater. Interfaces* **2020**, *12*, 15538.
[34] T. Kawabata, Y. Matsuo, *Mater. Sci. Appl.* **2018**, *9*, 779.
[35] T. Kawabata, *Proton Conductivity in Chitin System*, IntechOpen, London, UK **2021**.
[36] L. Xu, M. Rahmani, Y. Ma, D. A. Smirnova, K. Z. Kamali, F. Deng, Y. K. Chiang, L. Huang, H. Zhang, S. Gould, D. N. Neshev, A. E. Miroshnichenko, *Adv. Photonics* **2020**, *2*, 026003.
[37] S. H. Cho, K. M. Roccapriore, C. K. Dass, S. Ghosh, J. Choi, J. Noh, L. C. Reimnitz, S. Heo, K. Kim, K. Xie, B. A. Korgel, X. Li, J. R. Hendrickson, J. A. Hachtel, D. J. Milliron, *J. Chem. Phys.* **2020**, *152*, 014709.
[38] N. Borodinov, P. Banerjee, S. H. Cho, D. J. Milliron, O. S. Ovchinnikova, R. K. Vasudevan, J. A. Hachtel, *J. Chem. Phys.* **2021**, *154*, 014202.
[39] R. J. Mendelsberg, Y. Zhu, A. Anders, *J. Phys. D: Appl. Phys.* **2012**, *45*, 425302.
[40] S. L. Gibbs, C. M. Staller, A. Agrawal, R. W. Johns, C. A. Saez Cabezas, D. J. Milliron, *J. Phys. Chem. C* **2020**, *124*, 24351.